communications physics

A Nature Portfolio journal

Article

https://doi.org/10.1038/s42005-026-02565-z

Regularized micromagnetic theory for Bloch points

Vladyslav M. Kuchkin [1] ✉, Andreas Haller [1], Andreas Michels[1], Thomas L. Schmidt [1] & Nikolai S. Kiselev [2]

Magnetic singularities known as Bloch points (BPs) present a fundamental challenge for micromagnetic theory, which is based on the assumption of a fixed magnetization vector length. Due to the divergence of the effective field at a BP, classical micromagnetics fails to adequately describe BP dynamics. To address this issue, we propose a regularized micromagnetic model in which the magnetization vector can vary in length but not exceed a threshold value. More specifically, the magnetization is treated as an order parameter constrained to an $\mathbb{S}^3$-sphere. This constraint respects fundamental properties of local spin expectation values in quantum systems. We derive the corresponding regularized Landau-Lifshitz-Gilbert equation and the analog of the Thiele equation describing the steady motion of spin textures under various external stimuli. We demonstrate the applicability of our theory by modeling the dynamics of several magnetic textures containing BPs, including domain walls in nanowires, chiral bobbers, and magnetic dipolar strings. The presented results extend micromagnetic theory by incorporating a regularized description of BP dynamics.

Micromagnetism[1–4] is a well-established classical field theory that describes both static and dynamic properties of magnetic media, including bulk and nanoscale crystals, amorphous alloys, and heterostructures. The success of micromagnetism lies in its strong predictive power. It accurately describes, for example, the dynamics of domain walls, resonance spectra, magnetization reversal loops, and many other experimentally observed phenomena[4]. Micromagnetism has profoundly influenced the development of technologies based on magnetic materials, including computing devices[5–7], data storage[8–10], electric motors[11], and robotics[12,13].

In micromagnetism, the magnetization in a ferromagnet is considered a continuous three-dimensional vector field n(r), defined at every point r within the sample. Continuity of the magnetization field is a central assumption of micromagnetic theory–and, at the same time, one of its key limitations. It holds for a broad but nevertheless limited class of magnetic spin textures. In particular, only a few years after Brown formulated the foundations of micromagnetism[1], Feldtkeller[14] and Döring[15] independently demonstrated that, in certain configurations representing statically stable solutions of the micromagnetic Hamiltonian, this continuity is broken. The solutions they identified correspond to hedgehog-like vector fields, $\mathbf{n} = \mathbf{r}/r$, stabilized by boundary conditions in ball-shaped samples. Today, such point-like topological defects are commonly referred to as Bloch points (BPs).

Subsequent studies have shown that BPs can be stabilized under various conditions. For instance, BPs arise naturally during dynamic processes, such as the nucleation and annihilation of topologically non-trivial spin textures, including merons[16], skyrmions[17,18], and hopfions[19–21]. Therefore, a consistent theory that allows for the modeling of BP dynamics is essential for constructing a unified physical picture of topological magnetic solitons.

The existence of BPs and their mobility in the magnetic samples are supported by numerous direct and indirect experimental observations[22–46], and has a long history of theoretical study[47–90]. In contrast, describing BP dynamics remains a fundamental challenge for micromagnetic theory. The obstacle lies in the divergence of the effective field in the magnetization dynamics equation when a BP is present. This divergence stems directly from the constraint of constant magnetization magnitude. One of the earliest attempts to address the divergence of the effective field at magnetic singularities was made in Ref. 55. Their phenomenological approach is based on the Landau-Lifshitz-Bar'yakhtar[91] equation and introduces a Landau-type term, $\sim \chi(T)(\mathbf{n}^4 - 2\mathbf{n}^2)$, that incorporates temperature directly into the Hamiltonian via the parameter $\chi(T)$. While this method formally removes the divergence in the effective field by allowing the magnetization magnitude to vary near the core of a point singularity, it lacks a clear connection to the standard micromagnetic framework and to the classical Landau-Lifshitz-Gilbert (LLG) equation, which does not explicitly include temperature. Other approaches–such as those based on the Landau-Lifshitz-Bloch[92] equation and discussed in more detail in the Discussion section–suffer from the same limitation. In the present work, we extend the classical micromagnetic model by introducing a higher-dimensional order-

[1]Department of Physics and Materials Science, University of Luxembourg, Luxembourg, Luxembourg. [2]Peter Grünberg Institute, Forschungszentrum Jülich and JARA, Jülich, Germany. ✉e-mail: vladyslav.kuchkin@uni.lu

parameter space that naturally eliminates this divergence while preserving the core structure of the LLG equation. This results in a unified theoretical framework that consistently describes both smooth textures and configurations with singularities.

The fixed magnetization length assumed in the standard micromagnetic model for smooth textures is, in general, consistent with the results of quantum spin models. However recent studies have shown that quantum fluctuations remain significant in the vicinity of BPs[93–95]. These fluctuations can substantially reduce the length of observable classical spins, but cannot increase it. Thus, the magnetization must satisfy the inequality $|\mathbf{n}(\mathbf{r})|\leq 1$, rather than being strictly constrained to unit length. Such a relaxed constraint enables the use of an order parameter that remains regular even in the presence of BPs, thereby resolving the associated divergence. This motivated us to develop a regularized micromagnetic theory capable of describing textures both with and without BPs. Given the proven predictive power of classical micromagnetics, such a theory should reproduce all well-established results and modify only those solutions that contain BPs. Here, we present such a regularized micromagnetic theory.

In this study, we first formulate the problem and introduce the order parameter along with the regularized micromagnetic Hamiltonian, which we refer to as the $\mathbb{S}^3$-model. We then derive the dynamical equation for the $\mathbb{S}^3$-model, including the effects of external torques. Next, using the collective coordinate approach, we derive an analog of the Thiele equation describing the rigid motion of magnetic textures within this framework. The applicability of the derived equations is illustrated through examples of the dynamics of various BP-hosting spin textures. We also compare numerical simulations based on the $\mathbb{S}^3$-model and the standard micromagnetic model ($\mathbb{S}^2$-model) with analytical solutions of the Thiele equations. Finally, we discuss the topological properties of the $\mathbb{S}^3$-model, review earlier experiments on the dynamics of magnetic bubbles containing BPs, and address several frequently asked questions concerning our approach, its numerical implementation, and previously compare it with earlier attempts to regularize micromagnetic equations.

Results

In this study, we consider the following form of the micromagnetic Hamiltonian:

$$E=\int[e_{\mathrm{exi}}+e_{\mathrm{dmi}}+e_{\mathrm{ddi}}+e_{\mathrm{ani}}+e_{\mathrm{z}}]dV, \tag{1}$$

$\mathcal{D}\mathbf{n}\cdot\nabla\times\mathbf{n}$ is the Dzyaloshinskii-Moriya interaction (DMI), $e_{ani}=-\mathbf{n}\cdot\widehat{\mathcal{K}}\cdot\mathbf{n}$ is the magnetic anisotropy, $e_{ddi}=-\frac{1}{2}\mathcal{M}\mathbf{B}_d\cdot\mathbf{n}$ is the demagnetizing field interaction, and $e_z=-\mathcal{M}\mathbf{B}_{ext}\cdot\mathbf{n}$ is the Zeeman interaction with the external magnetic field. We denote the saturation magnetization by $\mathcal{M}$, and define the normalized magnetization as $\mathbf{n}=\mathbf{M}(r)/\mathcal{M}$. Then, the demagnetizing field $\mathbf{B}_\mathrm{d}$ can be found by solving the Maxwell equation $\nabla\cdot(\mathbf{B}_d+\mu_0\mathcal{M}\mathbf{n})=0$, which in practice is typically done using a scalar potential formulation[96] or an equivalent vector potential approach[97,98]. The Hamiltonian (1) can be straightforwardly extended to include additional interactions. We adopt this form of the Hamiltonian because it covers all example cases considered in this study.

Interestingly, the equation describing magnetization dynamics was established by Landau and Lifshitz[99] even before micromagnetic theory itself was formulated. Today, this equation is commonly referred to as the LLG equation. Its standard form, expressed in terms of the unit magnetization vector, is given by:

$$\dot{\mathbf{n}}=-\gamma\mathbf{n}\times\mathbf{b}-\alpha\gamma\mathbf{n}\times(\mathbf{n}\times\mathbf{b}), \tag{2}$$

where $\dot{\mathbf{n}}$ denotes the time derivative of the magnetization vector, $\gamma=\gamma_0/(1+\alpha^2)$, γ_0 is the electron gyromagnetic ratio, and α is the Gilbert damping constant. The effective field is defined as $\mathbf{b}=-\mathcal{M}^{-1}\delta E/\delta\mathbf{n}$, where E is the micromagnetic Hamiltonian (1). By definition, Eq. (2) preserves the magnitude of the magnetization vector. Applying it to a magnetic texture containing a BP inevitably leads to a divergence problem, which can be illustrated by considering only the exchange energy term in Eq. (1). The effective field due to exchange interaction is $\mathbf{b}_{exi}=-2\mathcal{A}\mathcal{M}^{-1}\nabla^2\mathbf{n}$. For hedgehog-like spin textures, $\mathbf{n}=\mathbf{r}/r$, it diverges $|\mathbf{b}_{\mathrm{exi}}|\sim 1/r^2$ as $r\to 0$. The only way to resolve the divergence problem is to allow the absolute value of magnetization to vary continuously, reaching $|\mathbf{n}|=0$ at $r=0$, i.e., at the core of the BP (see Supplementary note 1).

However, in this case, the order parameter no longer lies on the two-sphere $\mathbb{S}^2$, and one must introduce appropriate corrections to both the model Hamiltonian (1) and the LLG equation (2). The key question is on which manifold the order parameter should be defined.

Our previous study of BPs in the quantum spin model[95] showed that an effective micromagnetic model can be formulated in terms of a magnetization field defined on the three-sphere $\mathbb{S}^3$. In other words, the order parameter can be defined as a four-dimensional vector $\boldsymbol{\nu}=(\nu_1,\nu_2,\nu_3,\nu_4)$ constrained to $\mathbb{S}^3$, i.e., $|\boldsymbol{\nu}|=1$ at every point in the magnetic sample. The first three components of $\boldsymbol{\nu}$ correspond to the Cartesian components of the magnetization vector $\mathbf{n}$, while the fourth component encodes the magnetization length via the relation

$$\nu_1=n_x,\ \nu_2=n_y,\ \nu_3=n_z,\ \nu_4^2=1-|\mathbf{n}|^2. \tag{3}$$

As follows from (3), for $|\boldsymbol{\nu}|=1$, the magnetization satisfies the inequality $|\mathbf{n}|\leq 1$, and thus the magnetization can be reduced up to zero but never exceeds the maximal value ($|\mathbf{M}(\mathbf{r})|\leq\mathcal{M}$).

To rewrite the Hamiltonian (1) in terms of the order parameter $\boldsymbol{\nu}$, $E(\mathbf{n})\mapsto\mathcal{E}(\boldsymbol{\nu})$, we follow the approach of Ref. 95 and generalize only the Heisenberg exchange interaction, $e_{\mathrm{exi}}(\mathbf{n})\mapsto e_{\mathrm{exi}}(\boldsymbol{\nu})$, as follows:

$$e_{exi}(\boldsymbol{\nu})=\mathcal{A}\sum_{i=1}^{4}(\nabla\nu_i)^2+\kappa\nu_4^2. \tag{4}$$

All other terms in Eq. (1) are obtained by a straightforward substitution $(n_x,n_y,n_z)\mapsto(\nu_1,\nu_2,\nu_3)$ and thus do not depend on ν_4. In particular, for magnetostatic interactions in the $\mathbb{S}^3$-model, only the first three components of $\boldsymbol{\nu}$ contribute to the demagnetizing field $\mathbf{B}_\mathrm{d}$ which is a three dimensional vector that can be obtained from Maxwell's equation.

The phenomenological parameter κ in Eq. (4) is assumed to be positive and has units of J/m^3. Like all other material parameters, it is treated as a temperature-dependent quantity, $\kappa=\kappa(T)$. This parameter also serves to distinguish the auxiliary component ν_4 from the physically measurable components of the order parameter, ν_1, ν_2, and ν_3. We refer to ν_4 as auxiliary because it has no direct physical observable associated with it and is introduced solely to extend the order parameter space from $\mathbb{S}^2$ to $\mathbb{S}^3$ for regularization purposes.

The regularized form of the exchange energy term (4) ensures the continuity of the order parameter, even for hedgehog-like configurations. In such cases, the measurable components of the order parameter can vanish at the center of the texture and approach unity exponentially, as $\sim 1-\exp(-r/L_\kappa)$, far from the Bloch point[95]. The parameter $L_\kappa=\sqrt{\mathcal{A}/\kappa}$, which has units of length, can be interpreted as the characteristic size of the BP.

The effective field $\boldsymbol{\beta}(\boldsymbol{\nu})=-\mathcal{M}^{-1}(\delta\mathcal{E}/\delta\boldsymbol{\nu})$, acting on the four-dimensional vector $\boldsymbol{\nu}$, can be computed directly from the regularized Hamiltonian $\mathcal{E}(\boldsymbol{\nu})$. Together with $\boldsymbol{\nu}(\mathbf{r})$, the effective field $\boldsymbol{\beta}(\boldsymbol{\nu})$ remains continuous throughout the sample, even in the presence of BPs. In the next section, using the above expression for effective field and following the approach of Landau and Lifshitz[99], we derive a generalized dynamical equation for the order parameter $\boldsymbol{\nu}$.

Regularized dynamics equation

The LLG equation (2) has a simple geometric interpretation: it describes the motion of a point constrained to the surface of a two-sphere $\mathbb{S}^2$ [Fig. 1a]. In this case, $\dot{\mathbf{n}}$ is always perpendicular to $\mathbf{n}$ and lies in the tangent plane to the

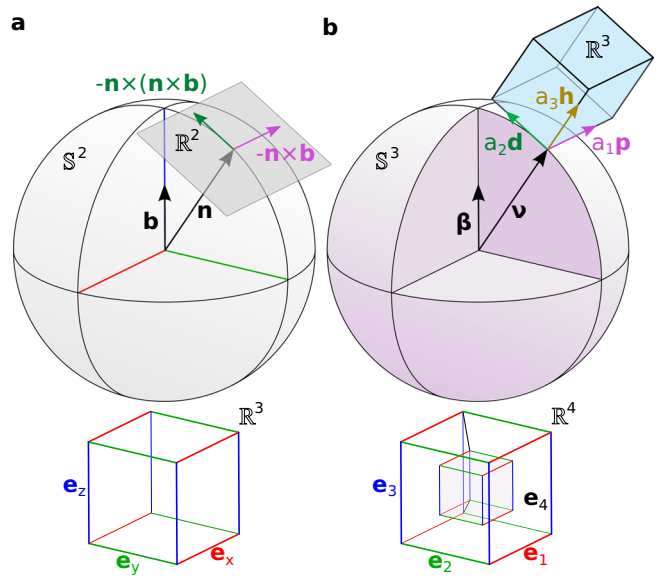

Fig. 1 | Geometric interpretation of the LLG equations in the $\mathbb{S}^2$ and $\mathbb{S}^3$ models. **a**,**b** illustrate the configuration spaces of the order parameter for the standard micromagnetic model constrained to the two-sphere $\mathbb{S}^2$, and the regularized model defined on the three-sphere $\mathbb{S}^3$, respectively. In (**a**) the three-dimensional unit vector **n** lies on the two-sphere embedded in $\mathbb{R}^3$ space. The associated tangent space $\mathbb{R}^2$ contains orthogonal directions corresponding to the conventional basis vectors: $\mathbf{n}\times\mathbf{b}$ (precession) and $\mathbf{n}\times(\mathbf{n}\times\mathbf{b})$ (damping). In (**b**) the four-dimensional unit vector $\boldsymbol{\nu}$ is defined on the three-sphere $\mathbb{S}^3$ embedded in $\mathbb{R}^4$ space. Note that in (**b**), the vectors $\boldsymbol{\nu}$, **p**, **d**, and **h** are mutually orthogonal in four-dimensional space; this orthogonality is represented schematically, as it cannot be faithfully depicted in a two-dimensional figure.

sphere, which is locally isomorphic to $\mathbb{R}^2$. Within this plane, $\dot{\mathbf{n}}$ is spanned by two orthogonal basis vectors: $-\mathbf{n}\times\mathbf{b}$ and $-\mathbf{n}\times(\mathbf{n}\times\mathbf{b})$, which are usually called *precession* and *dissipation* term, respectively. These vectors form a complete basis of the tangent space, and $\dot{\mathbf{n}}$ can be written as a linear combination of basis vectors (cf. Eq. (2)).

In the case of dynamics on the $\mathbb{S}^3$-sphere [Fig. 2b], the corresponding vector $\dot{\boldsymbol{\nu}}$ is perpendicular to $\boldsymbol{\nu}$ and lays in the tangent space of $\mathbb{S}^3$, which is locally isomorphic to $\mathbb{R}^3$. Within this $\mathbb{R}^3$ space, the vector $\dot{\boldsymbol{\nu}}$ can be spanned by three basis vectors, **p, d** and **h**, and can be written as linear combination:

$$\dot{\boldsymbol{\nu}} = a_1\mathbf{p} + a_2\mathbf{d} + a_3\mathbf{h}, \tag{5}$$

where a_1, a_2, a_3 are scalars that generally speaking can be functions of $\boldsymbol{\nu}$. The fact that the tangent space of $\mathbb{S}^3$ is well defined everywhere–including at points corresponding to vanishing magnetization–highlights the geometric advantage of using this manifold over the ball $\mathbb{B}^3 = \{\mathbf{n}, |\mathbf{n}| \le 1\}$, which may at first appear to be a reasonable choice. Since $\mathbb{S}^3$ is a compact and boundaryless manifold–just like the standard micromagnetic model defined on $\mathbb{S}^2$–it preserves a fixed norm of the extended order parameter while allowing for variable magnetization length. This enables a smooth and globally well-defined generalization of LLG dynamics, even in the presence of singularities. In contrast, a ball $\mathbb{B}^3$ has a boundary and a poorly defined tangent space at $|\mathbf{n}| = 0$, making it impractical for a consistent geometric formulation of the dynamics.

The basis vectors in (5) are required, by definition, to be mutually orthogonal and orthogonal to $\boldsymbol{\nu}$. Without loss of generality, we define the first basis vector **p** as a natural generalization of the precession term in Eq. (2), meaning it is chosen to be orthogonal to both $\boldsymbol{\nu}$ and $\boldsymbol{\beta}$. In four dimensions, however, this condition alone does not uniquely determine **p** – a third orthogonal direction must also be fixed. To resolve this ambiguity, we arbitrarily assume that **p** is orthogonal to the basis vector $\mathbf{e}_4$:

$$\mathbf{p} = \boldsymbol{\nu}\times\boldsymbol{\beta}\times\mathbf{e}_4. \tag{6}$$

The right-hand side of (6) denotes the Hodge dual of the wedge product, which is equivalent to computing the determinant of a 4×4 matrix whose upper row consists of the standard $\mathbb{R}^4$ basis vectors ($\mathbf{e}_1$, $\mathbf{e}_2$, $\mathbf{e}_3$, $\mathbf{e}_4$) and the next three rows contain components of the four-dimensional vectors $\boldsymbol{\nu}$, $\boldsymbol{\beta}$, and $\mathbf{e}_4 = (0, 0, 0, 1)$.

The second basis vector **d** is defined by analogy with the damping term in Eq. (2):

$$\mathbf{d} = \boldsymbol{\nu}(\boldsymbol{\nu}\cdot\boldsymbol{\beta}) - \boldsymbol{\beta}. \tag{7}$$

Since **d** is a linear combination of $\boldsymbol{\nu}$ and $\boldsymbol{\beta}$, both of which are orthogonal to **p**, it follows that **d** is also orthogonal to **p**. Finally, the third basis vector **h** is defined as orthogonal to $\boldsymbol{\nu}$, **p** and **d**:

$$\mathbf{h} = \boldsymbol{\nu}\times\mathbf{p}\times\mathbf{d}, \tag{8}$$

where, similar to (6), the right-hand side denotes the Hodge dual of the wedge product.

Our goal is to derive dynamical equations that reduce to the standard LLG equation (2) in the absence of BPs. By setting $\nu_4 = 0$ in Eqs. (6)–(8), we find that Eq. (5) recovers the standard LLG form when the prefactors are chosen as $a_1 = -\gamma$ and $a_2 = -\alpha\gamma$. The coefficient a_3 cannot be determined in this limiting case, as the vector **h** is quadratic in the effective field and has no counterpart in the standard LLG equation (2). To determine a_1 and a_2 in this limit, one must formally set a_3 to zero. For generality, we define $a_3 = \epsilon\gamma$, where ϵ is a phenomenological constant with units of 1/Tesla. It is worth emphasizing that ϵ is assumed to be a constant. Any possible functional dependence $\epsilon(\boldsymbol{\nu})$ would need to be derived from a more general microscopic theory beyond the phenomenological framework used here. Taking all of the above into account, the regularized LLG equation takes the form:

$$\dot{\boldsymbol{\nu}} = -\gamma\mathbf{p} - \alpha\gamma\mathbf{d} - \epsilon\gamma\,\boldsymbol{\nu}\times\mathbf{p}\times\mathbf{d}. \tag{9}$$

In the following, we demonstrate that, in the first approximation, the last term in Eq. (9) can be omitted. While the first two terms are linear in $|\boldsymbol{\beta}|$, the third one is quadratic. In Supplementary Note 2, we prove that it is impossible to construct **h** linear in components of $\boldsymbol{\beta}$. The fact that $|\mathbf{h}| \sim \mathcal{O}(\boldsymbol{\beta}^2)$ suggests that it might dominate at large $\boldsymbol{\beta}$. In practice, however, it is not the case. First, note that all three terms in Eq. (9) depend only on the component of the effective field orthogonal to $\boldsymbol{\nu}$, denoted $\boldsymbol{\beta}_\perp$. The longitudinal component, $\boldsymbol{\beta}_\parallel = (\boldsymbol{\nu}\cdot\boldsymbol{\beta})\boldsymbol{\nu}$, does not contribute to $\dot{\boldsymbol{\nu}}$, and we can replace $\boldsymbol{\beta}$ in Eqs.(6)–(8) with $\boldsymbol{\beta}_\perp = \boldsymbol{\beta} - (\boldsymbol{\nu}\cdot\boldsymbol{\beta})\boldsymbol{\nu}$. It can be seen that the first two terms scale linearly with $\boldsymbol{\beta}_\perp$, and the third term scales quadratically. Notably, a similar structure appears in the standard LLG equation, where both the precession and damping terms are linear in the transverse component of the effective field, $\mathbf{b}_\perp$. In micromagnetic theory, we study the states close to equilibrium, where $\boldsymbol{\nu}$ is nearly aligned with $\boldsymbol{\beta}$. In this regime, $\boldsymbol{\beta}_\perp$ is small, and higher-order terms in $\boldsymbol{\beta}_\perp$ can be neglected. In the far-from-equilibrium regime, where $\boldsymbol{\beta}_\perp$ is no longer small, the last term in (9) must be taken into account. Examples of such far-from-equilibrium processes include Bloch point nucleation and annihilation. Here, we focus on the dynamics of BPs that are already present in the system. Therefore, in the present study, we set $\epsilon = 0$. A complete treatment of the regularized LLG equation with $\epsilon \neq 0$ will be presented elsewhere.

While **d** and **h** differ in their structure–being linear and quadratic in the effective field $\boldsymbol{\beta}$, respectively–both torques contribute to changes in the magnetization length, as they depend on all components of $\boldsymbol{\nu}$. Only the precessional torque **p** is length-conserving, since it is orthogonal to $\boldsymbol{\nu}$ and does not contain ν_4.

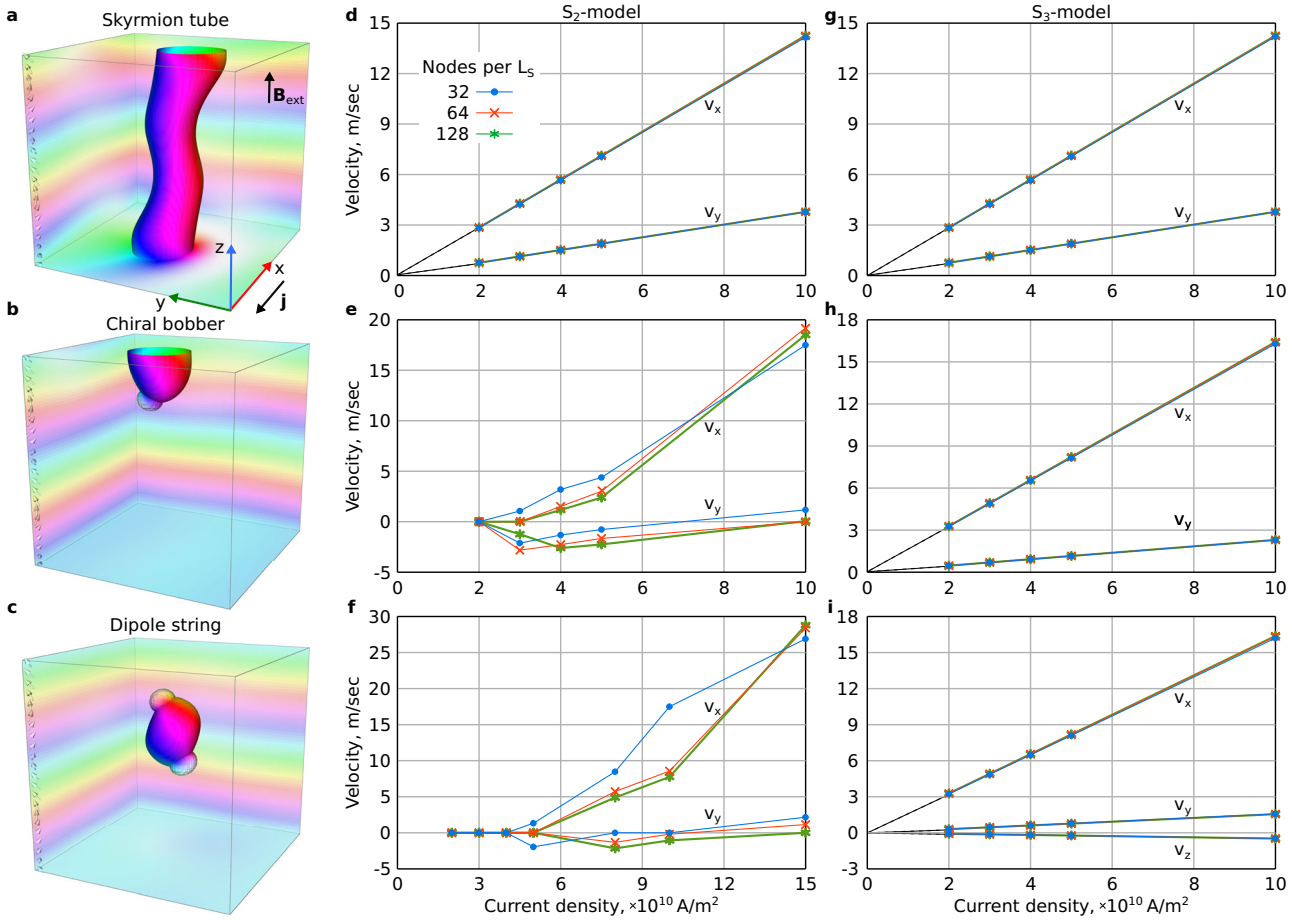

Fig. 2 | Current-induced dynamics of various magnetic solitons in chiral magnets. a–c show skyrmion tube, chiral bobber, and dipolar string, respectively. Corresponding magnetic texture are visualized by color-coded magnetization at the isosurfaces ($v_3 = 0$) and edges of the simulated domain. Additional isosurfaces having nearly spherical shapes indicate the position of BPs in (**b**) and (**c**) is given by $v_4 = 0.9$. The first column of plots in (**d–f**) show the velocity dependencies on the current density for skyrmion, chiral bobber, and dipole string, respectively, estimated from micromagnetic simulations based on the standard $\mathbb{S}^2$-model. The second column of plots in (**g–i**) shows velocity dependence estimated from micromagnetic simulations based on the regularized $\mathbb{S}^3$-model. Every plot contains velocities estimated in the simulations performed with different discretizations, see legend in (**d**). In the estimation of the solitons' velocity, we used the modified formulae for the calculation of the solitons' center, which automatically take into accountperiodic boundary conditions. For details, see the main text and Methods section on "Semi-analytical Thiele approach". Numerical source data for the graph are provided in Supplementary Data 1.

External torques

When external stimuli are applied, we must distinguish whether they are explicitly included in the Hamiltonian (1), such as a magnetic field gradient, or whether they must be directly incorporated into the LLG equation, for instance, as an electric current. In the former, the regularized LLG equation (9) can be used straightforwardly, and in the latter, the corresponding torques have to be added to (9). Here, we consider a practical example of Zhang-Li spin-transfer torque[100], which is often used to model the magnetization dynamics induced by an electric current. In case of standard LLG, we have to add to Eq. (2) the following term:

$$\mathbf{T} = -\frac{\xi-\alpha}{1+\alpha^2}\mathbf{n}\times(\mathbf{u}\cdot\nabla)\mathbf{n} + \frac{1+\xi\alpha}{1+\alpha^2}(\mathbf{u}\cdot\nabla)\mathbf{n}, \tag{10}$$

where $\mathbf{u} = \mu_B\mu_0\mathbf{j}/2e\gamma_0\mathcal{M}(1+\xi^2)$, $\mathbf{j}$ is the current density vector, and ξ is the non-adiabaticity parameter. To model this torque in the $\mathbb{S}^3$-model, we perform in Eq. (10) a mapping $\mathbf{n} \mapsto \boldsymbol{\nu}$ taking into account the constraint $|\boldsymbol{\nu}| = 1$ and equality $\boldsymbol{\nu}\cdot\dot{\boldsymbol{\nu}} = 0$ that must hold. The resulting expression for the Zhang-Li spin-transfer torque in $\mathbb{S}^3$-model can be written as follows:

$$\boldsymbol{\tau} = -\frac{\xi-\alpha}{1+\alpha^2}[\boldsymbol{\nu}\times(\mathbf{u}\cdot\nabla)\boldsymbol{\nu}\times\mathbf{e}_4] + \frac{1+\xi\alpha}{1+\alpha^2}(\mathbf{u}\cdot\nabla)\boldsymbol{\nu}, \tag{11}$$

where the expression in square brackets represents the Hodge dual of the wedge product as in Eqs. (6) and (8). A similar approach can be applied to generalize other torques in the regularized LLG equation.

It is worth mentioning that external torques are typically assumed to be small, resulting in "slow" magnetization dynamics. Capturing fast dynamical processes requires extending the LLG equation with higher-order terms, such as the nutation term[101,102], which lies beyond the scope of the present work. Here, we restrict our analysis to small torques and focus on the near equilibrium regime which can be described by the terms which are linear with respect to the effective field.

Collective coordinates approach

The steady-state dynamics of rigid magnetic textures moving at constant velocity $\mathbf{v}$ under external forces or torques is of particular interest in micromagnetic theory[9]. In such cases, the velocity of objects such as domain walls, skyrmions, or vortices can be obtained directly from the Thiele equation[103], an effective equation of motion derived using the collective coordinate approach. This method avoids solving the full LLG equation and eliminates the need for time-consuming micromagnetic simulations. Moreover, the solution of the Thiele equation can be considered an exact result toward which numerical simulations should converge in the limit of steady-state motion under weak driving forces. The collective coordinate approach assumes that the soliton's internal structure remains rigid and

does not undergo significant deformation–an assumption that naturally breaks down under strong perturbations. In the weak-driving regime, however, the texture deviates only slightly from the static configuration. In this case, to estimate the soliton velocity using the collective coordinate framework, it is sufficient to use the initial magnetization profile $\mathbf{n}(\mathbf{r}, t = 0)$, obtained via energy minimization. Here, we follow this approach and compare the resulting velocities with those obtained from full micromagnetic simulations, demonstrating consistency between the two methods. This agreement provides a valuable benchmark of both the numerical implementation and the underlying theoretical framework. Below we derive a generalized version of the Thiele equation for the $\mathbb{S}^3$-model.

First, we parametrize $\boldsymbol{\nu}$ using spherical coordinates on the three-sphere $\mathbb{S}^3$, denoted by angles Θ, Φ, and Ψ:

$$\boldsymbol{\nu} = \begin{pmatrix} \sin\Theta\cos\Phi\cos\Psi \\ \sin\Theta\sin\Phi\cos\Psi \\ \cos\Theta\cos\Psi \\ \sin\Psi \end{pmatrix}^T \tag{12}$$

Using this parametrization, we reformulate the regularized LLG equation (9) in terms of the spherical angles Θ, Φ, and Ψ (see Supplementary Note 3). In the case of rigid motion of a magnetic texture, the following relation holds: $\mathcal{R}(\mathbf{r}, t) = \mathcal{R}(\mathbf{r} - \mathbf{v}t)$ for $\mathcal{R} \in \Theta, \Phi, \Psi$. This implies that the time derivatives of the spherical angles are given by:

$$\dot{\Theta} = -\mathbf{v}\cdot\nabla\Theta,\ \dot{\Phi} = -\mathbf{v}\cdot\nabla\Phi,\ \dot{\Psi} = -\mathbf{v}\cdot\nabla\Psi. \tag{13}$$

The left-hand sides of these equations can be directly obtained from the regularized LLG equation derived in the previous step. Following the standard procedure[9], we next assume that during steady motion the total energy of the system remains constant. As a result, the dissipation function must vanish:

$$\int\left(\frac{\delta\mathcal{E}}{\delta\Theta}\nabla\Theta + \frac{\delta\mathcal{E}}{\delta\Phi}\nabla\Phi + \frac{\delta\mathcal{E}}{\delta\Psi}\nabla\Psi\right)dV = 0. \tag{14}$$

The combined solution of Eqs. (13) and (14) yields the Thiele equation (see Supplementary Note 4):

$$\alpha\,\mathbf{g}\times\mathbf{v} + \widehat{\gamma}\mathbf{v} = \mathbf{f}, \tag{15}$$

where the force due to the electric current is given by $\mathbf{f} = -\alpha\mathbf{g}\times\mathbf{u} - [(1+\xi\alpha)\widehat{\gamma} + (\xi-\alpha)\widehat{\gamma}']\mathbf{u}/(1+\alpha^2)$. Here, $\mathbf{g}$ is the gyrovector, and $\widehat{\gamma}$ and $\widehat{\gamma}'$ are the dissipation tensors, whose components are defined as follows:

$$\begin{aligned} g_i &= \epsilon_{ijk}\int\frac{\mathbf{n}\cdot\partial_j\mathbf{n}\times\partial_k\mathbf{n}}{n^2+\alpha^2}dV,\ \ \{i,j,k\}\in\{x,y,z\}, \\ \widehat{\gamma}_{jk} &= \int\frac{\alpha^2\partial_j\boldsymbol{\nu}\cdot\partial_k\boldsymbol{\nu} + \partial_j\nu_4\partial_k\nu_4}{n^2+\alpha^2}dV, \\ \widehat{\gamma}'_{jk} &= \alpha\int\frac{n^2\partial_j\boldsymbol{\nu}\cdot\partial_k\boldsymbol{\nu} - \partial_j\nu_4\partial_k\nu_4}{n^2+\alpha^2}dV. \end{aligned} \tag{16}$$

where ϵ_{ijk} is the Levi-Civita symbol. The derived Eq. (15) is applicable for electric currents $\mathbf{u}$ applied in arbitrary directions when the background magnetization is uniform, i.e., in a saturated state. However, when the vacuum corresponds to a non-uniform magnetic configuration, such as a spin spiral with wave vector $\mathbf{k}$, natural constraints on the current direction arise. In particular, to avoid excitation of the background magnetization, the current must lie in the plane orthogonal to the wave vector, i.e., $\mathbf{u}\perp\mathbf{k}$. These and related constraints on the motion of three-dimensional magnetic textures in non-uniform backgrounds were analyzed in detail in Ref. 104.

In the following examples, we set $\mathbf{k}\|\mathbf{e}_z$ and $\mathbf{u}\|\mathbf{e}_x$, so the current does not excite the background magnetization. Consequently, for the skyrmion string and the chiral bobber, the soliton velocity has no out-of-plane component: $\mathbf{v} = (v_x, v_y, 0)$. For fully 3D magnetic solitons—such as hopfions[105], dipolar strings[106], and hybrid skyrmion tubes[104]—this restriction no longer applies, allowing solitons to move in any direction. A general solution to the Thiele equation for this case is derived in Supplementary Note 5.

Finally, it is worth noting that setting $\nu_4 = 0$ in Eq. (15) reduces the equation to the standard Thiele equation:

$$\mathbf{G}\times\mathbf{v} + \alpha\Gamma\mathbf{v} = \mathbf{F}, \tag{17}$$

where the gyro-vector $\mathbf{G}$ has components $G_i = \int[\epsilon_{ijk}\mathbf{n}\cdot\partial_j\mathbf{n}\times\partial_k\mathbf{n}]dV$, the dissipation tensor Γ has components $\Gamma_{jk} = \int[\partial_j\mathbf{n}\cdot\partial_k\mathbf{n}]dV$, and $\mathbf{F}$ is an external force, which for the case of Zhang-Li torque is given by $\mathbf{F} = -\mathbf{G}\times\mathbf{u} - \xi\Gamma\mathbf{u}$.

Current-induced soliton dynamics

In this section, we present the results of numerical simulations on the dynamics of BP-hosting spin textures using the regularized LLG equation (9) with the Zhang-Li torque (11). These results are compared with simulations based on the standard LLG simulations in Mumax3[107]. Our implementation of the regularized LLG equation is available in a public repository[108], which represents a modified fork of the Mumax3 code. In addition to the regularized LLG equation, this fork includes several other advanced features. For example, it provides an implementation of the regularized geodesic nudged elastic band method for the $\mathbb{S}^3$ model, which we previously used in Ref. 106.

To illustrate the advantages of the regularized over the standard LLG equation, we consider a skyrmion tube [Fig. 2a], chiral bobber[109] [Fig. 2b], and dipole string[106] [Fig. 2c]. These solitons are representative examples of magnetic textures containing zero, one and two BPs, respectively. These solitons are stabilized in chiral magnets, where the natural background (vacuum) state is a helical or conical phase.

We consider a system of size $2L_e \times 2L_e \times 2L_e$, where L_e is the equilibrium period of chiral modulations. Note that L_e depends on the type of magnetic anisotropy. In isotropic systems ($\mathcal{K} = 0$), the equilibrium period is given by $L_D = 4\pi\mathcal{A}/\mathcal{D}$. In contrast, for systems with easy-plane anisotropy ($\mathcal{K}\neq 0$), there is no analytical solution, and L_e must be found numerically. The material parameters used to stabilize the skyrmion string and the chiral bobber are identical, whereas the dipolar string requires slightly different conditions (see Methods). Because of that, the value of L_e for the case of dipole string differs from that for skyrmion string and chiral bobber. For the skyrmion string and chiral bobber, we apply periodic boundary conditions in the xy-plane and open boundary conditions along the z-axis. In the case of the dipolar string, a fully 3D magnetic soliton, we model a bulk crystal and impose periodic boundary conditions in all three directions. In our simulations, we use discrete meshes of varying densities to demonstrate how the cuboid size influences Bloch point dynamics in both models (see legend in Fig. 2d).

In the case of the skyrmion string [Fig. 2d, g], simulations using both the standard and regularized LLG equations yield identical results. In both models, the skyrmion moves with the same deflection angle $\arctan(v_y/v_x)$. Importantly, the outcomes of these simulations are stable with respect to varying mesh density and show excellent agreement with analytical predictions from the Thiele equation (see Supplementary Table 1). In particular, as the current density $\mathbf{j}$ decreases, both the longitudinal (v_x) and transverse (v_y) components of the velocity decrease linearly and vanish in the limit $\mathbf{j}\to 0$.

In contrast to the skyrmion string case, the results for the chiral bobber and dipole string reveal substantial discrepancies between the standard and regularized micromagnetic models. In the standard $\mathbb{S}^2$-based model, the velocity exhibits a nonlinear dependence on the current density, with a nonzero critical current below which motion does not occur [Fig. 2e, f]. This behavior cannot be justified within the framework of continuum theory, where the magnetic medium is treated as continuous and free from intrinsic thresholds for magnetization dynamics. It also contradicts the Thiele

equation, which predicts a linear dependence of velocity on the current density. These artifacts indicate a fundamental failure of the standard micromagnetic model to correctly describe systems containing magnetic singularities. Moreover, simulations based on the $\mathbb{S}^2$-model do not exhibit convergence with increasing mesh density as in the case of skyrmion tube Fig. 2d, which makes them unreliable for studying Bloch point dynamics.

The most striking inconsistency observed in simulations of the chiral bobber and dipole string is the inverted skyrmion Hall angle upon varying current density and mesh discretization [see sign reversal of v_y in Fig. 2e, f]. Such behavior of the skyrmion Hall angle in micromagnetic simulations contradicts the Thiele equation (17) and thus represents an artifact. In continuum models, the sign of the skyrmion Hall angle is uniquely determined by the topological charge of the magnetic texture and remains invariant.

On the other hand, the regularized $\mathbb{S}^3$-based model consistently produces physically meaningful results that do not show noticeable dependence on the mesh density [Fig. 2h, i]. Similar to the case of skyrmion strings [Fig. 2g], the velocities linearly converge to zero with the current density, as predicted by the Thiele equation (15) (see Supplementary Table 1).

BP motion in a nanowire

In magnetic nanowires, a BP can appear at the center of a domain wall separating two oppositely magnetized domains aligned along the wire axis [Fig. 3a]. Such domain walls arise from the competition between the Heisenberg exchange interaction and the demagnetizing field. They have been extensively studied both experimentally[29,33,110–113] and theoretically[114–126]. In the following, we consider a soft magnetic material modeled by taking into account the Heisenberg exchange, demagnetizing field, and Zeeman energy terms. Under these conditions, the head-to-head domain wall structure depicted in Fig. 3a admits two energetically equivalent BP configurations, as shown in Fig. 3b, c. A key feature of these systems is that a weak external magnetic field can readily induce BP dynamics. The domain whose magnetization is aligned with the field expands, causing the domain wall and the enclosed BP to move along the wire. Here, we focus on the low-field, linear-response regime, where the dynamics can be well approximated by the rigid motion of the spin texture. Nonlinear effects, such as those associated with ultrafast domain wall motion[124], are beyond the scope of this work.

Figure 3 d and e show simulation results for BP dynamics under external fields ranging from 1 mT to 4 mT, using the standard and regularized micromagnetic models, respectively. The results from the standard LLG simulations reveal unphysical behavior. In particular, the response of the domain wall to an applied magnetic field exhibits oscillatory behavior. As shown in Supplementary Fig. 1, the temporal evolution of the magnetization components (n_x, n_y, n_z) exhibits oscillations with frequencies that cannot be explained within a continuum approximation. More importantly, Fig. 3d shows that increasing mesh density leads to a suppression of BP motion. Below a certain discretization threshold, the BP becomes fully pinned and stops moving. This implies that an unphysical numerical parameter—the mesh density—determines the behavior of the system. Equivalently, we can say that in the standard micromagnetic model, there exists a mesh density-dependent critical field below which BP does not move. Thereby, we conclude that such a pinning field is a numerical artifact, arising from the divergence of the effective field at the BP core in the standard micromagnetic model.

Although the results in Fig. 3d correspond to a specific parameter set, the observed BP pinning effect–whether due to increasing mesh resolution or decreasing external field–is a general artifact inherent to the standard micromagnetic model.

In contrast, the regularized $\mathbb{S}^3$-model is free from this issue [Fig. 3e]. Like the chiral bobber and dipolar string, the BP in this model exhibits smooth motion, with velocity continuously tending to zero as $B_{\text{ext}} \to 0$. Moreover, the BP dynamics in the regularized model do not induce any artificial magnetization oscillations (see Supplementary Fig. 1).

Discussions

On the κ-parameter

Micromagnetic theory operates on several characteristic length scales that depend on the material type and the dominant interactions. In uniaxial ferromagnets, this length is typically defined by the domain wall width[4], $L_c = \sqrt{2\mathcal{A}/(2\mathcal{K} + \mu_0\mathcal{M}^2)}$. In isotropic chiral magnets, the characteristic length corresponds to the equilibrium period of the spin spiral[17], $L_D = 4\pi\mathcal{A}/\mathcal{D}$, where $\mathcal{D}$ denotes the DMI constant. In the case of textures such as chiral kinks[127], a shorter characteristic length appears, $L_{\text{ck}} \sim 0.1L_{\text{D}}$. In exchange-frustrated systems, the characteristic scale is determined by the ratio of competing exchange terms[20].

In the regularized micromagnetic model, the size of the magnetic texture surrounding a point singularity (the "size" of the Bloch point) defines an additional characteristic length, $L_\kappa = \sqrt{\mathcal{A}/\kappa}$. To ensure the accuracy of numerical simulations, the discretization grid must be much smaller than the shortest relevant characteristic length. In the examples presented in the main text, κ was chosen such that L_κ is comparable to either L_c or L_D. In general, however, κ is determined by the properties of the specific material (lattice symmetry, sort of atoms, electron density of states, etc.) and does not necessarily correlate with the other characteristic lengths.

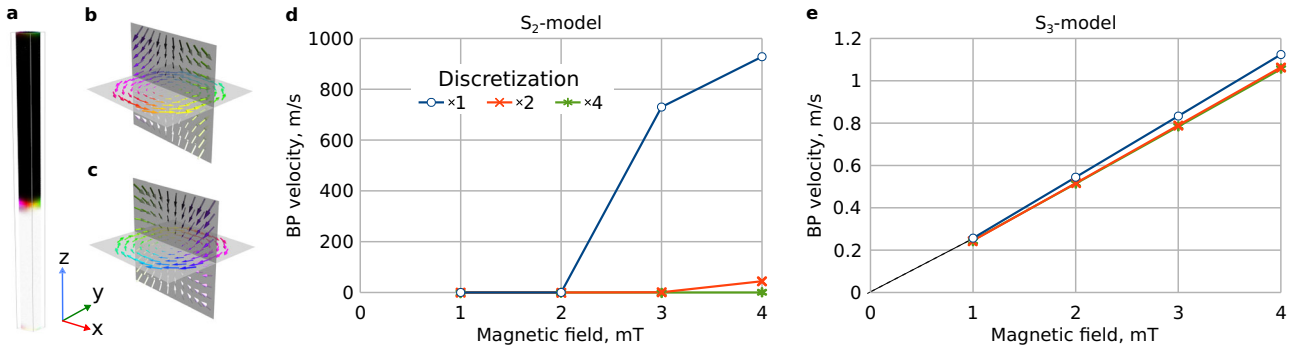

Fig. 3 | Bloch point dynamics in a nanowire. a A magnetic nanowire containing two domains magnetized along $+\mathbf{e}_z$ (white) and $-\mathbf{e}_z$ (black), which are separated by a domain wall containing a Bloch point (BP). In an external magnetic field $\mathbf{B}_{\text{ext}} \| \mathbf{e}_z$, the BP moves along the wire axis. Simulations were performed for two domain-wall configurations, shown in (**b**) and (**c**). Both configurations exhibit identical BP dynamics. **d** and (**e**) show the BP velocity as a function of the external magnetic field strength, computed using the standard and regularized LLG equations, respectively. Simulations were carried out at different discretization levels: × 1 corresponds to a 16 × 16 × 512 mesh, while × 2 and × 4 indicate uniform scaling of each spatial dimension by factors of 2 and 4, respectively. Domain size and material parameters are provided in the Methods section on "Micromagnetic simulations of BP in a nanowire". Numerical source data for the graph are provided in Supplementary Data 2.

Anisotropic systems

In the most general case, the exchange stiffness $\mathcal{A}$ is a second-rank symmetric tensor, which reduces to a scalar only in isotropic systems. In anisotropic systems, such as certain hexagonal crystals[128], multilayered structures[42,72,84], or van der Waals magnets[129], the exchange energy term should be written in a more general form:

$$e_{exi}(\boldsymbol{\nu}) = \sum_{j=x,y,z} \mathcal{A}_j \sum_{i=1}^{4} (\partial_j \nu_i)^2 + \kappa \nu_4^2.$$

In this case, the Bloch point may lose its spherical symmetry. As a result, the characteristic size of the magnetic point singularity becomes direction-dependent.

To determine the appropriate value of the regularization parameter κ for a given material, one must rely on experimental data or microscopic calculations based on more fundamental models, such as the quantum Heisenberg model or density functional theory[130]. While the design proposal of an experiment reaches beyond the scope of this study, we want to note that neutron scattering cross sections are sensitive to the norm of the magnetization[95], which could prove useful to estimate κ.

Classical spin lattice models

Magnetism is inherently of quantum mechanical origin, and quantum models offer the most fundamental framework for describing magnetic materials. However, the complexity of these models limits their applicability. In practice, we often have to rely on models with a significantly reduced number (order of thousands) of quantum particles or with magnetic spins approximated by classical vectors.

One such model is the quantum Heisenberg model, which treats spins as quantum objects but uses a simplified Hamiltonian. While this approach provides valuable insights[131,132], it is computationally limited to systems of about a few thousand spins. In contrast, real magnetic systems typically contain billions of spins.

The next level of simplification is classical spin lattice models. They can reproduce many experimental results and extend applicability to systems on the order of tens of nanometers. The applicability of classical atomistic spin models, where the magnetic moment has a fixed length, is justified only in certain limiting cases[133], and is generally regarded as a useful limiting approximation.

To reach micrometer scales, one usually employs the micromagnetic theory, which describes the classical spin lattice model in the continuum limit. Although its predictive power, micromagnetics inherits the limitations of classical spin lattice models and imposes an additional constraint of magnetic texture continuity. Most importantly, both approaches neglect the intrinsic quantum nature of spin.

An original multiscale approach aimed at describing Bloch-point dynamics was introduced by Hertel and Andreas[134,135]. Their method combines standard micromagnetic and atomistic spin-lattice models within a single computational framework. However, due to its inherent complexity, this approach has been less thoroughly examined with respect to agreement with experimental observations. By *inherent complexity*, we refer to the requirement that the three regions, each governed by its own Hamiltonian, must be translated coherently together with the BP position. Implementing such a framework may introduce additional artifacts at the interfaces between these regions. Most importantly, this type of multiscale approach does not overcome the fundamental limitations of micromagnetic theory discussed above.

The regularized micromagnetic model introduced here is not derived from the classical fixed-length spin lattice model and therefore avoids its inherent limitations. Instead, it accounts for the possibility of magnetization length reduction inherently present in more general quantum spin Hamiltonians. Accordingly, it is more appropriate to compare our model with such quantum atomistic models rather than classical spin models. Thereby, for the magnetic textures with singularities, our model is not expected to converge to classical atomistic spin dynamics. However, for smooth magnetic textures such as vortices, skyrmions, and hopfions, the regularized model agrees well with both classical micromagnetics and classical atomistic simulations.

Topological aspects of the problem

In the absence of singularities, where the extended order parameter $\boldsymbol{\nu}$ effectively reduces to the normalized magnetization vector $\mathbf{n} \in \mathbb{S}^2$, our model coincides with classical micromagnetic theory. In this regime, continuous spin textures can be classified using topological invariants such as the skyrmion and hopfion indices, associated with the homotopy groups $\pi_2(\mathbb{S}^2) = \mathbb{Z}$ and $\pi_3(\mathbb{S}^2) = \mathbb{Z}$, respectively. However, in the most general case where $\boldsymbol{\nu} \in \mathbb{S}^3$, the second homotopy group become trivial $\pi_2(\mathbb{S}^3) = 0$. The third homotopy group is non-trivial, $\pi_3(\mathbb{S}^3) = \mathbb{Z}$, but the associated topological invariant differs from the Hopf index and corresponds instead to the degree of a map $\mathbb{S}^3 \to \mathbb{S}^3$, as originally introduced in Skyrme's theory of baryons[136]. Thereby, the topological classification of magnetic textures via skyrmion and hopfion topological charges is inapplicable in this case.

Temperature in micromagnetism

According to the definition given by Landau, micromagnetism is an *athermal* theory[4]. It means that temperature enters the model Hamiltonian only implicitly — through the temperature dependence of material parameters such as saturation magnetization $\mathcal{M}$, anisotropy tensor $\widehat{K}$, exchange stiffness $\mathcal{A}$, and DMI constant $\mathcal{D}$. This reflects a key point: as long as the system exhibits a magnetic order, regardless of the particular temperature, the Hamiltonian (1) remains valid for describing its physical behavior. On the other hand, as the temperature approaches the Curie point T_c, the model may fail to capture effects driven by entropy and thermal fluctuations. However, as long as $T \ll T_c$, the entropy contribution to the free energy is assumed to be minimal. For most practical problems addressed by micromagnetics, it is sufficient to assume that the material parameters in (1) are functions of temperature.

At elevated temperatures near the Curie point ($T \simeq T_c$), the magnitude of the saturation magnetization can be modeled using a Landau expansion[55], $e_L = an^2 + bn^4$, which captures the characteristics of a second-order phase transition[137]. In this regime, two well-established dynamical equations have been proposed: the Landau-Lifshitz-Bloch (LLB) equation[92], derived from the Fokker-Planck formalism, and the phenomenological Landau-Lifshitz-Baryakhtar (LLBar) equation[91]. Both frameworks serve as generalizations of the LLG equation, incorporating additional terms that allow for temporal variations in the magnitude of the magnetization. This leads to a natural question: can these models be used to describe BP dynamics by treating the temperature-dependent parameters as free constants, even without considering temperature effects? Below, we outline several reasons why this approach is not suitable.

First, the Landau energy term does not inherently enforce the constraint $|\mathbf{n}| \leq 1$. As a result, the model permits unphysical increases in the magnetization magnitude beyond saturation. Regardless of how rare such deviations may be, the mere possibility of violating this fundamental constraint limits the applicability of the model to a narrow parameter range.

Second, while there were efforts to incorporate spin torques into the LLB equation[138], there is no established method for doing that for arbitrary torques that ensures the constraint $|\mathbf{n}| \leq 1$, which is crucial for physically consistent modeling. In contrast, the approach developed in this work naturally accommodates such torques. We explicitly demonstrate this by including the spin-transfer torque induced by spin-polarized electric currents.

Third, the experimentally observed dynamics of Bloch point-hosting spin textures (e.g., hard magnetic bubbles) are well described by the Thiele equation. This equation can be derived from the regularized LLG framework proposed here, but not from the LLB or LLBar equations.

In conclusion, there is no clear advantage in employing the Landau energy term and LLB or LLBar dynamics for modeling Bloch point behavior. The $\mathbb{S}^3$-based formulation offers a more consistent and physically

grounded framework, particularly for systems where the magnetization length varies due to quantum effects rather than thermal fluctuations. Unlike LLB and LLBar models, which allow unbounded magnetization length–effectively treating $\mathbf{n}$ as a vector in $\mathbb{R}^3$–our approach enforces the constraint $|\mathbf{n}|\leq 1$ by construction and naturally incorporates external torques without violating this constraint. Although establishing a formal connection between our model and LLB-type theories may be possible, such a mapping would not be straightforward and may not hold physical meaning especially in the low-temperature regime.

Methods

Micromagnetic simulations of soliton dynamics

To stabilize the skyrmion tube, chiral bobber, and dipole string (Fig. 2a–c), we consider the following Hamiltonian for chiral magnets:

$$\mathcal{E}_1 = \int [e_{exi} + e_{dmi} + e_{ani} + e_z] dV, \tag{18}$$

with the following parameters: $\mathcal{A} = 4$ pJ/m, $\mathcal{D} = 0.718$ mJ/m^2, $\mathcal{M} = 384$ kA/m^3. These parameters correspond to a spin-spiral period of $L_\mathrm{D} = 70$ nm. We further assume the $\kappa = 10^{-4}\mathcal{D}^2/2\mathcal{A}$ which corresponds to a characteristic BP size of $L_\kappa \approx 7.9$ nm. To stabilize skyrmion and chiral bobber, we apply an external field of $0.7\mathcal{D}^2/(2\mathcal{A}\mathcal{M})$, which corresponds to the equilibrium period of spin-spiral $L_\mathrm{e} = L_\mathrm{D}$. To stabilize dipole string we apply an external field of $0.55\mathcal{D}^2/(2\mathcal{A}\mathcal{M})$ and additionally add easy-plane anisotropy of strength $K_{u,xx} = -0.25\mathcal{D}^2/2\mathcal{A}$ (hard axis along x), that results in $L_\mathrm{e} \approx 1.016 L_\mathrm{D}$. The soliton motion was excited by electric current of density $\mathbf{j} = j\mathbf{e}_x$ of various strengths, where we fixed $\alpha = 0.05$ and $\xi = 0.25$. Numerical simulations were performed using the Mumax3 software for which we implemented the regularized LLG equation (9) with Zhang-Li torque (11)[108].

Semi-analytical Thiele approach

To compare the results of micromagnetic simulations with the predictions of the Thiele equation (15), we extracted information about skyrmion velocities from the simulation data. The position of soliton center, $\mathbf{r}_\mathrm{c}$, taking into account PBC was calculated as follows[106,139]:

$$r_{i,c} = \frac{L_i}{2\pi}\tan^{-1}\frac{\int \mathcal{N}_{jk}\sin(2\pi r_i/L_i)dr_i}{\int \mathcal{N}_{jk}\cos(2\pi r_i/L_i)dr_i} \pm l_i L_i, \tag{19}$$

where the non-repeating indices are cartesian coordinate components, $\{i, j, k\} \in \{x, y, z\}$, and $\mathcal{N}_{jk} = \int(1 - n_z)dr_j dr_k$, and where L_x, L_y and L_z denote the size of simulation domain. The integers l_i represent the number of times the soliton has crossed the domain boundary in the x, y, and z directions, respectively. Both solutions of Thiele's equation and numerical simulations shown in Fig. 2 suggest a linear dependency between the solitons' velocity components and the current density, $v_i = -c_i u$, where the dimensionless coefficient c_i is given by the solution of the Thiele equation. In Supplementary Table 1, we provide numerical values of this coefficient.

Micromagnetic simulations of BPs in a nanowire

We considered an Fe nanowire of length 1.2 μm and of diameter 35 nm which can be described by the Hamiltonian:

$$\mathcal{E}_2 = \int [e_{exi} + e_{ddi} + e_z] dV, \tag{20}$$

with $\mathcal{A} = 21$ pJ/m and $\mathcal{M} = 1.7$ MA/m. For the $\mathbb{S}^3$-model, we set $\kappa = 0.5$ MJ/m^3 that corresponds to a characteristic BP size of $L_\kappa = \sqrt{\mathcal{A}/\kappa} = 42$ nm. The initial configuration shown in Fig. 2a is stabilized at zero external field. To initiate domain wall motion, a magnetic field is applied along the wire, $B_\mathrm{ext} \| \mathbf{e}_z$. In both the standard and regularized LLG simulations, we use the same damping parameter, $\alpha = 0.01$. The position of the Bloch point, z_p, is estimated as:

$$z_p = \frac{\int r_z[n_x^2 + n_y^2]dV}{\int [n_x^2 + n_y^2]dV}, \tag{21}$$

that always provides us with a finite value as long as the domain wall is present in the wire.

Data availability

Source data for micromagnetic simulations and scripts for post-processing are available at https://doi.org/10.5281/zenodo.17474662.

Received: 29 July 2025; Accepted: 17 February 2026;
Published online: 11 March 2026

References

1. Brown, W. F. *Micromagnetics* (Interscience Publishers, 1963).
2. Aharoni, A. *Introduction to the Theory of Ferromagnetism*. (Clarendon Press, 2000).
3. Chikazumi, S. & Graham, C. D. *Physics of Ferromagnetism*. (Oxford University Press, 1997).
4. Hubert, A. & Schäfer, R. *Magnetic Domains: the Analysis of Magnetic Microstructures* (Springer, 2008).
5. Chumak, A. V., Serga, A. A. & Hillebrands, B. Magnon transistor for all-magnon data processing. *Nat. Commun.* **5**, 4700 (2014).
6. Parkin, S. S. P., Hayashi, M. & Thomas, L. Magnetic domain-wall racetrack memory. *Science* **320**, 190–194 (2008).
7. Wolf, S. A. et al. Spintronics: a spin-based electronics vision for the future. *Science* **294**, 1488–1495 (2001).
8. O' Dell, T. H. Magnetic bubble domain devices. *Rep. Prog. Phys.* **49**, 589 (1986).
9. Malozemoff, A. & Slonczewski, J. C. *Magnetic Domain Walls in Bubble Materials: Advances in Materials and Device Research*, vol. 1 (Academic Press, 1979).
10. Victora, R. & Shen, X. Exchange coupled composite media for perpendicular magnetic recording. *IEEE Trans. Magn.* **41**, 2828–2833 (2005).
11. Coey, J. Permanent magnet applications. *J. Magn. Magn. Mater.* **248**, 441–456 (2002).
12. Huang, H.-W., Sakar, M. S., Petruska, A. J., Pané, S. & Nelson, B. J. Soft micromachines with programmable motility and morphology. *Nat. Commun.* **7**, 12263 (2016).
13. Wu, S. et al. Evolutionary algorithm-guided voxel-encoding printing of functional hard-magnetic soft active materials. *Adv. Intell. Syst.* **2**, 202000060 (2020).
14. Feldtkeller, E. Mikromagnetisch stetige und unstetige magnetisierungskonfigurationen. *Z. f.ür. Angew. Phys.* **19**, 530–536 (1965).
15. Döring, W. Point singularities in micromagnetism. *J. Appl. Phys.* **39**, 1006–1007 (1968).
16. Rybakov, F. N., Eriksson, O. & Kiselev, N. S. Topological invariants of vortices, merons, skyrmions, and their combinations in continuous and discrete systems. *Phys. Rev. B* **111**, 134417 (2025).
17. Bogdanov, A. N. & Yablonskii, D. A. Thermodynamically stable "vortices" in magnetically ordered crystals. the mixed state of magnets. *Sov. Phys. JETP* **68**, 101 (1989).
18. Tokura, Y. & Kanazawa, N. Magnetic skyrmion materials. *Chem. Rev.* **121**, 2857–2897 (2020).
19. Voinescu, R., Tai, J.-S. B. & Smalyukh, I. I. Hopf solitons in helical and conical backgrounds of chiral magnetic solids. *Phys. Rev. Lett.* **125**, 057201 (2020).
20. Rybakov, F. N. et al. Magnetic hopfions in solids. *APL Mater.* **10**, 99942 https://doi.org/10.1063/5.0099942 (2022).
21. Zheng, F. et al. Hopfion rings in a cubic chiral magnet. *Nature* **623**, 718–723 (2023).

22. Slonczewski, J. C. Properties of bloch points in bubble domains. In *AIP Conference Proceedings* **24**, 613–614 (AIP, 1975). https://doi.org/10.1063/1.30197.
23. Jantz, W., Slonczewski, J. & Argyle, B. Effects of bloch lines and bloch points on resonances of magnetic bubbles. *J. Magn. Magn. Mater.* **23**, 8–14 (1981).
24. Argyle, B. E., Maekawa, S., Dekker, P. & Slonczewski, J. C. Gradientless propulsion and state switching of bubble domains. In *AIP Conference Proceedings*, 131–137 (American Institute of Physics, 1976). https://doi.org/10.1063/1.2946038.
25. Bullock, D. C. The effect of a constant in-plane magnetic field on magnetic bubble translation in. In *MAGNETISM AND MAGNETIC MATERIALS - 1973: Nineteenth Annual Conference*, 232-236 (ASCE, 1974). https://doi.org/10.1063/1.2947324.
26. Hasegawa, R. Effect of bloch points on the dynamic properties of bubble domain. In *AIP Conference Proceedings*, vol. 24, 615–616 (AIP, 1975). https://doi.org/10.1063/1.30198.
27. Josephs, R. M., Stein, B. F. & Bekebrede, W. R. Bubble domain translational motion in the presence of an in-plane field. *AIP Conference Proc.* 29, 65–66 (AIP, 1976). https://doi.org/10.1063/1.30506.
28. Milde, P. et al. Unwinding of a skyrmion lattice by magnetic monopoles. *Science* **340**, 1076–1080 (2013).
29. Da Col, S. et al. Observation of bloch-point domain walls in cylindrical magnetic nanowires. *Phys. Rev. B* **89**, 180405 (2014).
30. Jamet, S. et al. Quantitative analysis of shadow x-ray magnetic circular dichroism photoemission electron microscopy. *Phys. Rev. B* **92**, 144428. https://doi.org/10.1103/PhysRevB.92.144428 (2015).
31. Im, M.-Y. et al. Dynamics of the bloch point in an asymmetric permalloy disk. *Nat. Commun.* **10**, 593 (2019).
32. Zheng, F. et al. Experimental observation of chiral magnetic bobbers in b20-type fege. *Nat. Nanotechnol.* **13**, 451–455 (2018).
33. Wartelle, A. et al. Bloch-point-mediated topological transformations of magnetic domain walls in cylindrical nanowires. *Phys. Rev. B* **99**, 024433. https://doi.org/10.1103/PhysRevB.99.024433. (2019).
34. Álvaro-Gómez, L. et al. Topological analysis and experimental control of transformations of domain walls in magnetic cylindrical nanowires. *Phys. Rev. Res.* **7**, 023092 (2025).
35. Wohlhüter, P. et al. Nanoscale switch for vortex polarization mediated by bloch core formation in magnetic hybrid systems. *Nat. Commun.* **6**, 8836 (2015).
36. Kanazawa, N. et al. Critical phenomena of emergent magnetic monopoles in a chiral magnet. *Nat. Commun.* **7**, 11622 (2016).
37. Donnelly, C. et al. Three-dimensional magnetization structures revealed with x-ray vector nanotomography. *Nature* **547**, 328–331 (2017).
38. Donnelly, C. et al. Experimental observation of vortex rings in a bulk magnet. *Nat. Phys.* **17**, 316–321 (2020).
39. Han, H.-S. et al. Topology-dependent stability of vortex-antivortex structures. *Appl. Phys. Lett.* **118**, 212407 https://doi.org/10.1063/5.0045593 (2021).
40. Schöbitz, M. et al. Time-resolved imaging of Ersted field induced magnetization dynamics in cylindrical magnetic nanowires. *Appl. Phys. Lett.* **118**, 172411 https://doi.org/10.1063/5.0046643 (2021).
41. Arekapudi, S. S. P. K. et al. Direct imaging of distorted vortex structures and magnetic vortex annihilation processes in ferromagnetic/antiferromagnetic disk structures. *Phys. Rev. B* **103**, 014405 (2021).
42. Grelier, M. et al. Three-dimensional skyrmionic cocoons in magnetic multilayers. *Nat. Commun.* **13**, 6843 (2022).
43. Savchenko, A. S. et al. Diversity of states in a chiral magnet nanocylinder. *APL Mater.* **10**, 97650 (2022).
44. Yasin, F. S. et al. Bloch point quadrupole constituting hybrid topological strings revealed with electron holographic vector field tomography. *Adv. Mater.* **36**, 11737 https://doi.org/10.1002/adma.202311737 (2024).
45. Han, H.-S. et al. Manipulation of the magnetic monopole injection for topological transition. *NPG Asia Mater.* **16**, 9 https://doi.org/10.1038/s41427-024-00529-9 (2024).
46. Kern, L. et al. Controlled formation of skyrmion bags. *Adv. Mater.* **37**, 2501250 (2025).
47. Hubert, A. Mikromagnetisch singuläre punkte in bubbles. *J. Magn. Magn. Mater.* **2**, 25–31 (1975).
48. Arrott, A., Heinrich, B. & Aharoni, A. Point singularities and magnetization reversal in ideally soft ferromagnetic cylinders. *IEEE Trans. Magn.* **15**, 1228–1235 (1979).
49. Aharoni, A. Exchange energy near singular points or lines. *J. Appl. Phys.* **51**, 3330–3332 (1980).
50. Sokalski, K. Spin configurations near singularities in micromagnetism. *Phys. Lett. A* **75**, 491–492 (1980).
51. Kufaev, Y. A. & Sonin, E. B. Vibrations of a bloch line with a bloch point. *Fiz. Tverd. Tela* **30**, 3272–3275 (1988).
52. Kufaev, Y. A. & Sonin, E. B. Dynamics of a bloch point (point soliton) in a ferromagnet. *Zh. Eksp. Teor. Fiz.* **95**, 1523–1529 (1989).
53. Kabanov, Y. P., Dedukh, L. M. & Nikitenko, V. I. Bloch points in an oscillating bloch line. *Pis.Zh. Eksp. Teor. Fiz.* **49**, 551–554 (1989).
54. Kufaev, Y. A. & Sonin, E. B. Effects of magnetostatic stray fields on the dynamics and interaction of bloch points. *Zh. Eksp. Teor. Fiz.* **101**, 1550–1560 (1992).
55. Galkina, E., Ivanov, B. & Stephanovich, V. Phenomenological theory of bloch point relaxation. *J. Magn. Magn. Mater.* **118**, 373–378 (1993).
56. Thiaville, A. & Miltat, J. Controlled injection of a singular point along a linear magnetic structure. *Europhys. Lett.* **26**, 57–62 (1994).
57. Forster, H. et al. Domain wall motion in nanowires using moving grids (invited). *J. Appl. Phys.* **91**, 6914–6919 (2002).
58. Thiaville, A., García, J. M., Dittrich, R., Miltat, J. & Schrefl, T. Micromagnetic study of bloch-point-mediated vortex core reversal. *Phys.Rev. B* **67**, 094410 (2003).
59. Van Waeyenberge, B. et al. Magnetic vortex core reversal by excitation with short bursts of an alternating field. *Nature* **444**, 461–464 (2006).
60. Komineas, S. Rotating vortex dipoles in ferromagnets. *Phys. Rev. Lett.* **99**, 117202 (2007).
61. Volkov, V. V. & Bokov, V. A. Domain wall dynamics in ferromagnets. *Phys. Solid State* **50**, 199–228 (2008).
62. Elías, R. G. & Verga, A. Magnetization structure of a bloch point singularity. *Eur. Phys. J. B* **82**, 159–166 (2011).
63. Lebecki, K. M., Hinzke, D., Nowak, U. & Chubykalo-Fesenko, O. Key role of temperature in ferromagnetic bloch point simulations. *Phys. Rev. B* **86**, 094409 (2012).
64. Pylypovskyi, O. V., Sheka, D. D. & Gaididei, Y. Bloch point structure in a magnetic nanosphere. *Phys. Rev. B* **85**, 224401 (2012)..
65. Zverev, V. V. & Filippov, B. N. Transition micromagnetic structures in asymmetric vortexlike domain walls (static solutions and dynamic reconstructions). *J. Exp. Theor. Phys.* **117**, 108–120 (2013).
66. Schütte, C. & Rosch, A. Dynamics and energetics of emergent magnetic monopoles in chiral magnets. *Phys. Rev. B* **90**, 174432 (2014).
67. Andreas, C., Gliga, S. & Hertel, R. Numerical micromagnetism of strong inhomogeneities. *J. Magn. Magn. Mater.* **362**, 7–13 (2014).
68. Carvalho-Santos, V., Elías, R. & Nunez, A. Spin wave vortex from the scattering on bloch point solitons. *Ann. Phys.* **363**, 364–370 (2015).
69. Pylypovskyi, O. V., Sheka, D. D., Kravchuk, V. P. & Gaididei, Y. Vortex polarity switching in magnets with surface anisotropy. *Low. Temp. Phys.* **41**, 361–374 (2015).
70. De Lucia, A., Litzius, K., Krüger, B., Tretiakov, O. A. & Kläui, M. Multiscale simulations of topological transformations in magnetic-skyrmion spin structures. *Phys. Rev. B* **96**, 020405 (2017).

71. Ackerman, P. J. & Smalyukh, I. I. Diversity of knot solitons in liquid crystals manifested by linking of preimages in torons and hopfions. *Phys. Rev. X* **7**, 011006 (2017).
72. Beg, M. et al. Stable and manipulable bloch point. *Sci. Rep.* **9**, 2 (2019).
73. Charilaou, M. Prediction of confined and controllable bloch points in nanocubes of chiral magnets. *Phys. Rev. B* **102**, 014430 (2020).
74. Müller, G. P., Rybakov, F. N., Jónsson, H., Blügel, S. & Kiselev, N. S. Coupled quasimonopoles in chiral magnets. *Phys. Rev. B* **101**, 184405 (2020).
75. Gorobets, O., Gorobets, Y., Tiukavkina, I. & Gerasimenko, R. Spin-polarized current-driven ferromagnetic domain wall motion with a skyrmion-like building block. *Ukrainian J. Phys.* **65**, 919 (2020).
76. Pathak, S. A. & Hertel, R. Three-dimensional chiral magnetization structures in fege nanospheres. *Phys. Rev. B* **103**, 104414 https://doi.org/10.1103/physrevb.103.104414 (2021).
77. De Riz, A. et al. Mechanism of fast domain wall motion via current-assisted bloch-point domain wall stabilization. *Phys. Rev. B* **103**, 054430 https://doi.org/10.1103/PhysRevB.103.054430(2021).
78. Birch, M. T. et al. Topological defect-mediated skyrmion annihilation in three dimensions. *Commun. Phys.* **4**, 4 https://doi.org/10.1038/s42005-021-00675-4 (2021).
79. Azhar, M., Kravchuk, V. P. & Garst, M. Screw dislocations in chiral magnets. *Phys. Rev. Lett.* **128**, 157204 (2022).
80. Sáez, G., Díaz, P., Vidal-Silva, N., Escrig, J. & Vogel, E. E. Bloch points stabilization by means of diameter modulations in cylindrical nanowires. *Results Phys.* **39**, 105768 (2022).
81. Kuchkin, V. M. et al. Heliknoton in a film of cubic chiral magnet. *Front. Phys.* **11**, 1201018 https://doi.org/10.3389/fphy.2023.1201018 (2023).
82. Zambrano-Rabanal, C. et al. Magnetostatic interaction between bloch point nanospheres. *Sci. Rep.* **13**, 34167 https://doi.org/10.1038/s41598-023-34167-y (2023).
83. Castillo-Sepúlveda, S. et al. Nucleation and stability of toron chains in non-centrosymmetric magnetic nanowires. *Nanomaterials* **13**, 1816 (2023).
84. Lang, M., Beg, M., Hovorka, O. & Fangohr, H. Bloch points in nanostrips. *Sci. Rep.* **13**, 33998 https://doi.org/10.1038/s41598-023-33998-z (2023).
85. Qiu, L., Shen, L. & Shen, K. Spin-wave-driven tornado-like dynamics of three-dimensional topological magnetic textures. *Commun. Phys.* **7**, 116 https://doi.org/10.1038/s42005-024-01608-7 (2024).
86. Hermosa-Muñoz, J. et al. Hyperbolic bloch points in ferrimagnetic exchange spring. *Results Phys.* **61**, 107771 (2024).
87. Kim, S. T., Han, H.-S., Im, M.-Y. & Je, S.-G. Control of a twisted domain wall motion supported by topology. *J. Appl. Phys.* **135**, 0187965 https://doi.org/10.1063/5.0187965 (2024).
88. Shimizu, K., Okumura, S., Kato, Y. & Motome, Y. Current-induced motion of nanoscale magnetic torons over the wide range of the hall angle. *Commun. Phys.* **8**, 69 https://doi.org/10.1038/s42005-025-01970-0 (2025).
89. Yastremsky, I. A. Magnetization length in the bloch point at finite temperatures. *J. Magn. Magn. Mater.* **616**, 172834 (2025).
90. Winkler, T. B., Beg, M., Lang, M., Kläui, M. & Fangohr, H. Simulating bloch points using micromagnetic and heisenberg models. *IEEE Trans. Magn.* **61**, 1–8 (2025).
91. Baryakhtar, V. Phenomenological description of relaxation processes in magnets. *ZHurnal Eksperimentalnoi I Teoreticheskoi Fiziki* **87**, 1501–1508 (1984).
92. Garanin, D. A. Fokker-planck and Landau-lifshitz-bloch equations for classical ferromagnets. *Phys. Rev. B* **55**, 3050–3057 (1997).
93. Elías, R. G., Carvalho-Santos, V. L., Núñez, A. S. & Verga, A. D. Spin waves scattering on a bloch point. *Phys. Rev. B* **90**, 224414 https://doi.org/10.1103/PhysRevB.90.224414 (2014).
94. Tapia, A., Saji, C., Roldán-Molina, A. & Nunez, A. S. Stability enhancement by zero-point spin fluctuations: a quantum perspective on bloch point topological singularities. *Adv. Funct. Mater.* **34**, 12721 https://doi.org/10.1002/adfm.202312721 (2024).
95. Kuchkin, V. M. et al. Quantum and classical magnetic bloch points. *Phys. Rev. Res.* **7**, 013195 https://doi.org/10.1103/PhysRevResearch.7.013195 (2025).
96. Hubert, A. & Schäfer, R.*Magnetic domains: the analysis of magnetic microstructures* (Springer, 1998).
97. Di Fratta, G., Muratov, C. B., Rybakov, F. N. & Slastikov, V. V. Variational principles of micromagnetics revisited. *SIAM J. Math. Anal.* **52**, 3580–3599 (2020).
98. Zheng, F. et al. Magnetic skyrmion braids. *Nat. Commun.* **12**, 5316 (2021).
99. Landau, L. D. & Lifshitz, E. M. On the theory of the dispersion of magnetic permeability in ferromagnetic bodies. *Physikalische Z. der Sowjetunion* **8**, 153 (1935).
100. Zhang, S. & Li, Z. Roles of nonequilibrium conduction electrons on the magnetization dynamics of ferromagnets. *Phys. Rev. Lett.* **93**, 127204 https://doi.org/10.1103/PhysRevLett.93.127204 (2004).
101. Bajpai, U. & Nikolić, B. K. Time-retarded damping and magnetic inertia in the landau-lifshitz-gilbert equation self-consistently coupled to electronic time-dependent nonequilibrium green functions. *Phys. Rev. B* **99**, 69 https://doi.org/10.1103/PhysRevB.99.134409 (2019).
102. Mondal, R. et al. Inertial effects in ultrafast spin dynamics. *J. Magn. Magn. Mater.* **579**, 170830 (2023).
103. Thiele, A. A. Steady-state motion of magnetic domains. *Phys. Rev. Lett.* **30**, 230–233 (1973).
104. Kuchkin, V. M. & Kiselev, N. S. Homotopy transitions and 3D magnetic solitons. *APL Mater.* **10**, 071102 https://doi.org/10.1063/5.0097559 (2022).
105. Liu, Y., Hou, W., Han, X. & Zang, J. Three-dimensional dynamics of a magnetic hopfion driven by spin transfer torque. *Phys. Rev. Lett.* **124**, 127204 https://doi.org/10.1103/PhysRevLett.124.127204 (2020).
106. Kuchkin, V. M. et al. Stability and nucleation of dipole strings in uniaxial chiral magnets. *Phys. Rev. B* **111**, 174410 https://doi.org/10.1103/PhysRevB.111.174410 (2025).
107. Vansteenkiste, A. et al. The design and verification of mumax3. *AIP Adv.* **4**, 4899186 https://doi.org/10.1063/1.4899186 (2014).
108. Kuchkin, V. M. Regularized LLG simulations MuMax3 (extension). https://github.com/kuchkin/mumax3-gneb (2022).
109. Rybakov, F. N., Borisov, A. B., Blügel, S. & Kiselev, N. S. New type of stable particlelike states in chiral magnets. *Phys. Rev. Lett.* **115**, 117201 https://doi.org/10.1103/PhysRevLett.115.117201 (2015).
110. Fert, A. & Piraux, L. Magnetic nanowires. *J. Magn. Magn. Mater.* **200**, 338–358 (1999).
111. Biziere, N. et al. Imaging the fine structure of a magnetic domain wall in a ni nanocylinder. *Nano Lett.* **13**, 2053–2057 (2013).
112. Schöbitz, M. et al. Fast domain wall motion governed by topology and Ersted fields in cylindrical magnetic nanowires. *Phys. Rev. Lett.* **123**, 217201 https://doi.org/10.1103/PhysRevLett.123.217201 (2019).
113. Ruiz-Gómez, S. et al. Tailoring the energy landscape of a bloch point domain wall with curvature. *Nat Commun* **16**, 7422 https://doi.org/10.1038/s41467-025-62705-x (2025).
114. Hertel, R. & Kirschner, J. Magnetic drops in a soft-magnetic cylinder. *J. Magn. Magn. Mater.* **278**, L291–L297 (2004).
115. Thiaville, A. & Nakatani, Y.*Domain-Wall Dynamics in Nanowiresand Nanostrips*, 161–205 (Springer, 2006). https://doi.org/10.1007/10938171_5.
116. Hertel, R. Ultrafast domain wall dynamics in magnetic nanotubes and nanowires. *J. Phys. Condens. Matter* **28**, 483002 (2016).

117. Charilaou, M., Braun, H.-B. & Löffler, J. F. Monopole-induced emergent electric fields in ferromagnetic nanowires. *Phys. Rev. Lett.* **121**, 097202 (2018).
118. Ma, X.-P., Zheng, J., Piao, H.-G., Kim, D.-H. & Fischer, P. Cherenkov-type three-dimensional breakdown behavior of the bloch-point domain wall motion in the cylindrical nanowire. *Appl. Phys. Lett.* **117**, 013002 https://doi.org/10.1063/5.0013002 (2020).
119. Charilaou, M. Bloch point dynamics in exchange-spring heterostructures. *APL Mater.* **10**, 097610 https://doi.org/10.1063/5.0097610 (2022).
120. Moreno, R., Carvalho-Santos, V., Altbir, D. & Chubykalo-Fesenko, O. Detailed examination of domain wall types, their widths and critical diameters in cylindrical magnetic nanowires. *J. Magn. Magn. Mater.* **542**, 168495 (2022).
121. Fernandez-Roldan, J. A. & Chubykalo-Fesenko, O. Dynamics of chiral domain walls under applied current in cylindrical magnetic nanowires. *APL Mater.* **10**, 103408 (2022).
122. Askey, J., Hunt, M., Langbein, W. & Ladak, S. Asymmetric dual bloch point domain walls in cylindrical magnetic nanowires. *APL Mater.* **10**, 071105 (2022).
123. Fernandez-Roldan, J. A., P. del Real, R., Bran, C., Vazquez, M. & Chubykalo-Fesenko, O. Electric current and field control of vortex structures in cylindrical magnetic nanowires. *Phys. Rev. B* **102**, 024421 (2020).
124. Tejo, F., Fernandez-Roldan, J. A., Guslienko, K. Y., Otxoa, R. M. & Chubykalo-Fesenko, O. Giant supermagnonic bloch point velocities in cylindrical ferromagnetic nanowires. *Nanoscale* **16**, 10737–10744 (2024).
125. Bittencourt, G. H. R., Carvalho-Santos, V. L., Chubykalo-Fesenko, O., Altbir, D. & Moreno, R. Dynamics of chiral domain walls in bent cylindrical magnetic nanowires. *J. Appl. Phys.* **135**, 188985 (2024).
126. Saugar, E., Moreno, R., Chubykalo-Fesenko, O. & Guslienko, K. Topology-driven complex magnetization dynamics of the bloch-point domain wall in cylindrical geometry. *Phys. Rev. Appl.* **23**, 064028 (2025).
127. Kuchkin, V. M. et al. Magnetic skyrmions, chiral kinks, and holomorphic functions. *Phys. Rev. B* **102**, 144422 (2020).
128. Grundy, P., Hothersall, D., Jones, G., Middleton, B. & Tebble, R. The formation and structure of cylindrical magnetic domains in thin cobalt crystals. *Phys. Status Solidi* **9**, 79–88 (1972).
129. Han, M.-G. et al. Topological magnetic-spin textures in two-dimensional van der waals cr2ge2te6. *Nano Lett.* **19**, 7859–7865 (2019).
130. Szilva, A. et al. Quantitative theory of magnetic interactions in solids. *Reviews of Modern Phys.* **95**, 035004 (2023).
131. Haller, A., Groenendijk, S., Habibi, A., Michels, A. & Schmidt, T. L. Quantum skyrmion lattices in heisenberg ferromagnets. *Phys. Rev. Res.* **4**, 043113 (2022).
132. Rózsa, L., Wuhrer, D., Díaz, S. A., Nowak, U. & Belzig, W. Hidden quantum correlations in the ground states of quasiclassical spin systems. *Phys. Rev. B* **111**, 174441 (2025).
133. Millard, K. & Leff, H. S. Infinite-spin limit of the quantum heisenberg model. *J. Math. Phys.* **12**, 1000–1005 (1971).
134. Hertel, R. & Andreas, C.*Multiscale simulation of Bloch point dynamics in thick nanowires*, 653–677 (Elsevier, 2015). https://doi.org/10.1016/b978-0-08-100164-6.00022-9.
135. Andreas, C.*Multiscale Multimodel Simulation of Micromagnetic Singularities*, vol. 88 of *Schriften des Forschungszentrums Jülich. Reihe Schlüsseltechnologien / Key Technologies* (Forschungszentrum Jülich, 2014).Dissertation, Universität Duisburg-Essen/Université de Strasbourg.
136. Skyrme, T. H. R. A nonlinear field theory. *Proc. R. Soc. Lond. Ser. A, Math. Phys. Sci.* **260**, 127–138 (1961).
137. Landau, L. D. On the theory of phase transitions. *Zh. Eksp. Teor. Fiz.* **7**, 19–32 (1937).
138. Schieback, C., Hinzke, D., Kläui, M., Nowak, U. & Nielaba, P. Temperature dependence of the current-induced domain wall motion from a modified landau-lifshitz-bloch equation. *Phys. Rev. B* **80**, 214403 (2009).
139. Kuchkin, V. M. et al. Geometry and symmetry in skyrmion dynamics. *Phys. Rev. B* **104**, 165116 https://doi.org/10.1103/PhysRevB.104.165116 (2021).

Acknowledgements

N.S.K. and V.M.K. acknowledge F. N. Rybakov for fruitful discussions and critical comments. V.M.K., A.H., T.L.S., and A.M. acknowledge financial support from the National Research Fund of Luxembourg (AFR/23/17951349 and C22/MS/17415246/DeQuSky). V.M.K. acknowledges financial support from the European Union's Horizon Europe research and innovation program under the Marie Skłodowska-Curie grant agreement No. 101203692 (QUANTHOPF). N.S.K. acknowledges support from the European Research Council under the European Union's Horizon 2020 Research and Innovation Program (Grant No. 856538—project "3D MAGiC").

Author contributions

V.M.K. and N.S.K. conceived the project. V.M.K. developed the theoretical model and performed numerical simulations. V.M.K., A.H., A.M., T.L.S., and N.S.K. discussed the results and contributed to writing the manuscript.

Competing interests

The authors declare no competing interests.

Additional information

Supplementary information The online version contains supplementary material available at https://doi.org/10.1038/s42005-026-02565-z.

Correspondence and requests for materials should be addressed to Vladyslav M. Kuchkin.

Peer review information - *Communications Physics* thanks the anonymous reviewers for their contribution to the peer review of this work. A peer review file is available.